CHAPTER IV
RESULTS AND DISCUSSION

4.1 Synthesis and basic characterization of Fe(III) Schiff base complexes

4.1.1 Spectroscopic study of [Fe(salRen-5-OMe)$_2$]A

The infrared spectra of [Fe(salBzen-5-OMe)$_2$]A and [Fe(salPren-5-OMe)$_2$]A complexes are shown in Figures 4.1 and 4.2, with the corresponding IR spectroscopic data shown in Table 4.1. All complexes in this series exhibit similar spectra with the same key bands. The C=N stretches, corresponding to the imine groups in salBzen-5-OMe and salPren-5-OMe, appear around 1620-1631 cm^{-1}. The C=C stretches of the aromatic ring are observed in the range of 1463-1544 cm^{-1}, while N-H stretches are detected between 3087-3245 cm^{-1}. The benzyl group is more electron-withdrawing than the propyl group. This electron-donating effect of the propyl group reduces the strength of the C=C bonds in the aromatic ring and the C=N bonds in the complex. Consequently, the IR peaks of [Fe(salPren-5-OMe)$_2$]A **6**-**10** are comparatively lower in wavenumber than those of the [Fe(salBzen-5-OMe)$_2$]A **1**-**5** complexes. Additionally, the complexes show characteristic anion stretches for NO_3^- and ClO_4^- at 1290-1382 and 1085-1112 cm^{-1}, respectively (Díaz-Torres et al., 2020). The IR spectra are fully consistent with the proposed structures. However, complex **6** exhibits a broad band around 3409 cm^{-1}, which is attributed to O-H vibrational stretches, suggesting possible water absorption by the complex.

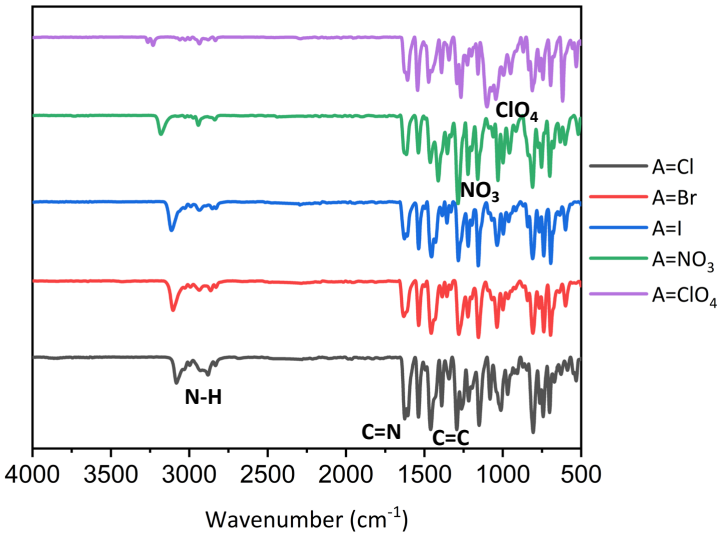

Figure 4.1 IR spectra of [Fe(salBzen-5-OMe)$_2$]A complexes.

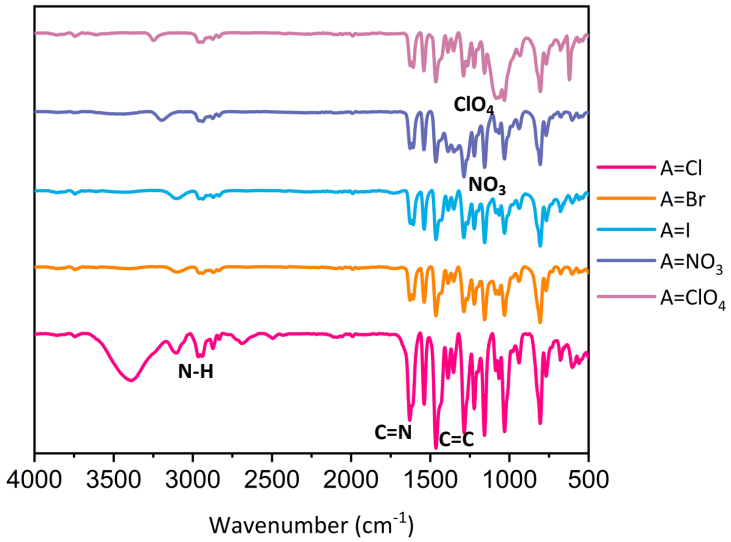

Figure 4.2 IR spectra of [Fe(salPen-5-OMe)$_2$]A complexes.

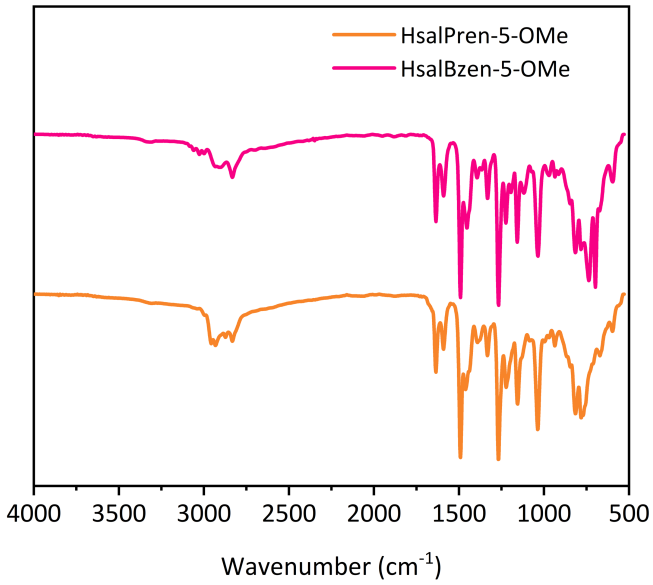

Figure 4.3 IR spectra of HsalPren-5-OMe and HsalBzen-5-OMe ligands.

Additionally, the infrared spectra of HsalPren-5-OMe and HsalBzen-5-OMe ligands exhibit characteristic vibrational bands corresponding to their functional groups (Figure 4.3). Both ligands show a broad absorption band in the region of 3000 cm^{-1}, which can be attributed to C-H stretching vibrations. A strong absorption band near 1500 cm^{-1} is associated with aromatic C=C stretching, while the C=N stretching vibrations of the imine groups in HsalPren-5-OMe and HsalBzen-5-OMe appear at approximately 1630 cm^{-1}. These spectral differences highlight the structural variations between the two ligands and their electronic effects.

Table 4.1 IR spectroscopic data of [Fe(salRen-5-OMe$_2$]A complexes.

Complexes	Wavenumber (cm^{-1})			
	ν_{N-H}	$\nu_{C=N}$	$\nu_{C=C}$	ν_{anion}
[Fe(salBzen-5-OMe$_2$]Cl **1**	3087	1629	1544	-
[Fe(salBzen-5-OMe$_2$]Br **2**	3105	1629	1537	-
[Fe(salBzen-5-OMe$_2$]I **3**	3112	1623	1535	-
[Fe(salBzen-5-OMe$_2$]NO_3 **4**	3178	1631	1542	1382
[Fe(salBzen-5-OMe$_2$]ClO_4 **5**	3232	1629	1542	1112
[Fe(salPren-5-OMe$_2$]Cl **6**	3107	1627	1463	-
[Fe(salPren-5-OMe$_2$]Br **7**	3190	1620	1463	-
[Fe(salPren-5-OMe$_2$]I **8**	3097	1620	1463	-
[Fe(salPren-5-OMe$_2$]NO_3 **9**	3190	1620	1463	1290
[Fe(salPren-5-OMe$_2$]ClO_4 **10**	3245	1622	1463	1085

The UV-Vis spectra of [Fe(salBzen-5-OMe$_2$]A and [Fe(salPren-5-OMe$_2$]A complexes in chloroform are shown in Figures 4.4-4.5. All complexes exhibit a prominent absorption band in the UV region, below 400 nm, is assigned to a charge transfer and intraligand π-π^* transitions arising from the aromatic ring of the salBzen and salPren ligands. In the visible region, two additional peaks are observed around 600 nm and 730 nm, likely corresponding to ligand-to-metal charge transfer (LMCT) bands from a phenolate p_π orbital to an iron(III) d_π orbital, as shown in Table 4.2. The λ_{max} positions are consistent with those observed in high spin Fe(III) complexes, such as $[Fe(salRen)_2]^+$ (Petty et al., 1978). These spectral values are consistent with those reported for various Fe(III) complexes, including [Fe(salMeen-5-Br$_2$]ClO_4, [Fe(salMeen-5-Cl$_2$]ClO_4 (Al-Azzani et al., 2020), [Fe(hapMen$_2$]ClO_4, [Fe(hapEen$_2$]ClO_4 (Shongwe et al., 2012), and [Fe(X-salMeen$_2$]PF_6 (Petty et al., 1978). In each case, the lower-energy band is indicative of the low-spin (LS) state, while the higher-energy band is characteristic of the high-spin (HS) state (Tweedle et al., 1976).

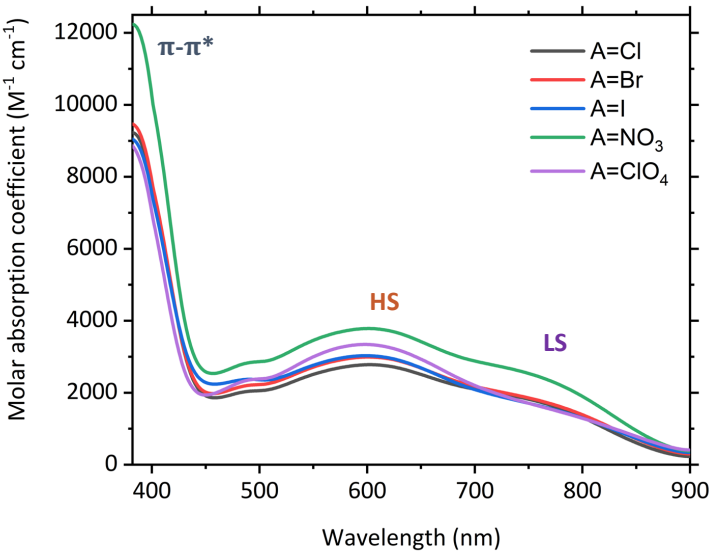

Figure 4.4 UV-Vis spectra of [Fe(salBzen-5-OMe)$_2$]A complexes.

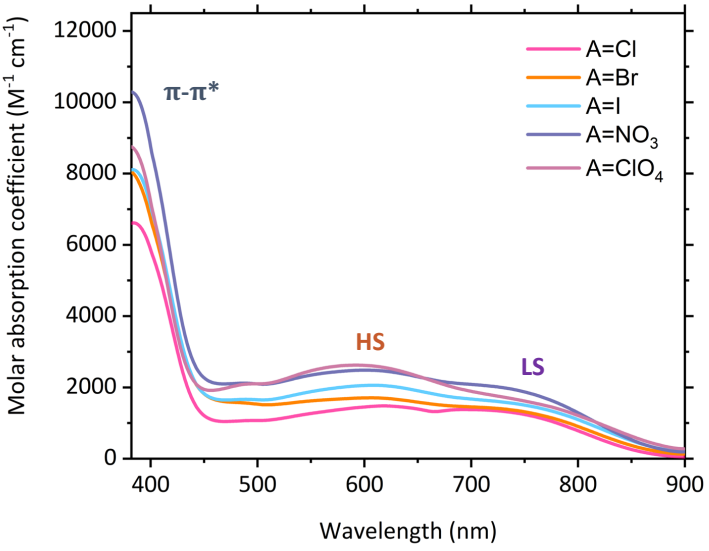

Figure 4.5 UV-Vis spectra of [Fe(salPren-5-OMe)$_2$]A complexes.

Table 4.2 UV-vis spectroscopic data of [Fe(salRen-5-OMe$_2$]A complexes.

Complexes	λ_{max} (nm), ε (M^{-1} cm^{-1})			
	π-π*	HS-LMCT	LS-LMCT	ε Ratio (HS/LS)
[Fe(salBzen-5-OMe$_2$]Cl **1**	385(7340)	606(2711)	738(1859)	1.46
[Fe(salBzen-5-OMe$_2$]Br **2**	389(7310)	605(2922)	739(1875)	1.56
[Fe(salBzen-5-OMe$_2$]I **3**	391(7626)	606(3127)	737(1866)	1.67
[Fe(salBzen-5-OMe$_2$]NO_3 **4**	384(7821)	601(3537)	733(2312)	1.53
[Fe(salBzen-5-OMe$_2$]ClO_4 **5**	380(7763)	604(4156)	732(2324)	1.79
[Fe(salPren-5-OMe$_2$]Cl **6**	390(6382)	596(1604)	731(1432)	1.12
[Fe(salPren-5-OMe$_2$]Br **7**	387(6856)	597(1693)	729(1357)	1.25
[Fe(salPren-5-OMe$_2$]I **8**	390(6977)	599(2051)	727(1601)	1.28
[Fe(salPren-5-OMe$_2$]NO_3 **9**	390(7607)	604(2441)	735(1914)	1.27
[Fe(salPren-5-OMe$_2$]ClO_4 **10**	388(7130)	605(2536)	732(1678)	1.51

The observed differences in the ε (HS/LS) ratios between the two series are consistent with variations in ligand field strength. The salPren-5-OMe ligand appears to induce a stronger ligand field, favoring the LS state, while the salBzen-5-OMe ligand supports a weaker ligand field, favoring the HS state. These differences might arise from electronic or steric effects introduced by the structural differences between salBzen and salPren ligands. However, the anion also impacts these ratios with the complexes increasingly LS as the N-H···anion interactions become stronger. The order of the anions is consistent with the Hofmeister series (Kang et al., 2020).

The elemental analysis and mass spectrometry data for complexes **1**-**10** confirmed their purity, as detailed in the experimental section and supporting information. It was observed that [Fe(salPren-5-OMe$_2$]A **6**-**10** contained 0.25 mol of H_2O, likely due to residual solvent from the synthesis process. Unfortunately, for compound **6**, the mass spectrometry data revealed a discrepancy between the molecular weight of the salPren ligand and the expected molecular weight of the complex. This discrepancy may result

from water absorption by the complex, which was observed as an oil-like sample. Despite extensive efforts to recrystallize the salPren series, no crystals suitable for SC-XRD were obtained. Furthermore, the powder X-ray diffraction (PXRD) data for these samples were broad and nearly amorphous. Although reasonable PXRD patterns were obtained for complexes **6**–**10** from extremely fresh samples, the difficulty in crystallization persisted, and most samples used for bulk measurements remained amorphous as shown in supporting information. In contrast, the [Fe(salBzen-5-OMe)$_2$]A (**1**–**5**) series did not contain any solvent. All complexes in this series successfully recrystallized, allowing for more definitive structural analysis. Additionally, the PXRD patterns of each complex in salBzen series align with their corresponding simulated patterns generated using Jana 2020 as shown in supporting information.

4.2 Structural studies of Fe(III) Schiff base complexes

Crystals of [Fe(salBzen-5-OMe)$_2$]Cl (**1**), [Fe(salBzen-5-OMe)$_2$]Br (**2**) and [Fe(salBzen-5-OMe)$_2$]I (**3**) were grown from CH_2Cl_2/hexane. While crystals of [Fe(salBzen-5-OMe)$_2$]NO_3 (**4**) and [Fe(salBzen-5-OMe)$_2$]ClO_4 (**5**) were grown from $CHCl_3$/hexane to give black blocks. They crystallize in monoclinic $P2_1/n$ or $P2_1/c$ (**1, 4** and **5**), monoclinic $P2_1/n$ (**2**) or tetragonal $P4_32_12$ (**3**) phases. The structures of **1**, **3** and **4** were determined at 150 and 295 K, while **2** was recorded at 295 K only. Efforts to determine the structure of **2** at low temperature were unsuccessful because of crystal cracking. In contrast, The unique magnetic characteristics of 5 (vide infra) motivated us to examine its structures at 30, 100 and 295 K. The Fe-ligand bond lengths and octahedral distortion parameters, calculated using OctaDist (Ketkaew et al., 2021), and the crystallographic data and refinement parameters are provided in Tables 4.3-4.6. In all cases, the Fe(III) center is six-coordinate, bonded to four nitrogen and two oxygen atoms from two meridional salBzen ligands, with the oxygen atoms positioned cis to each other, resulting in an octahedral coordination sphere (Figure 4.6-4.10). The anion is stabilized by N-H···anion interactions, with distances varying between 2.1 and 2.6 Å, varying with the anion size. Interestingly, in **1** symmetry-breaking

is observed, showing one independent HS Fe(III) centre at high temperature (295 K), and two centres (Fe1 and Fe2) at low temperature (150 K) that remain in a [HS-HS] state. The Fe-N/O bond lengths in **1** and **2** are in the ranges 2.161–2.180 Å and 1.902–1.921 Å, respectively, and are comparable to the corresponding distances observed for the HS Fe(III) center in $[Fe(naphBzen)_2]I$ found in the [LS-HS] state at 100 K and [HS-HS] state at 120 K (Boonprab et al., 2019). Even at low temperature, **1** exhibits no significant variation in bond distances. While Fe1 is much more distorted than Fe2, this suggests that **1** does not exhibit SCO down to 150 K. In contrast, $[Fe(salEen\text{-}Br)_2]Cl{\cdot}0.5H_2O$ also features two independent centers; however, at 150 K, one adopts the HS state while the other remains in the LS state (Cardoso et al., 2015). This suggests that salBzen-5-OMe displays a weaker ligand field than salEen-Br with the same anion. In contrast, the Fe N/O bond lengths for **3** and **4** are on average between 1.990-2.003 Å and 1.858-1.870 Å respectively, which is characteristic of LS Fe(III) at 150 K and 295 K, nevertheless, at 295 K the value remains slightly lower than anticipated for a fully HS state, suggesting an incomplete and gradual SCO within the examined temperature range. Interestingly, for **5** the Fe-O bond length remains relatively unchanged between 30 K and 100 K, indicating minimal structural rearrangement around the Fe-O coordination sphere in this temperature range. In contrast, the Fe-N bond lengths show a significant increase during this interval, reflecting notable changes in the Fe-N bond lengths (Figure 4.11). This behavior aligns with the complex's predominant HS state, even at 30 K. The elongation of Fe-N bonds corresponds to the HS state, while the stable Fe-O bond length highlights the structural rigidity of the Fe-O coordination. This structural observation supports the magnetic data, confirming the complex's strong preference for the HS state over the examined temperature range.

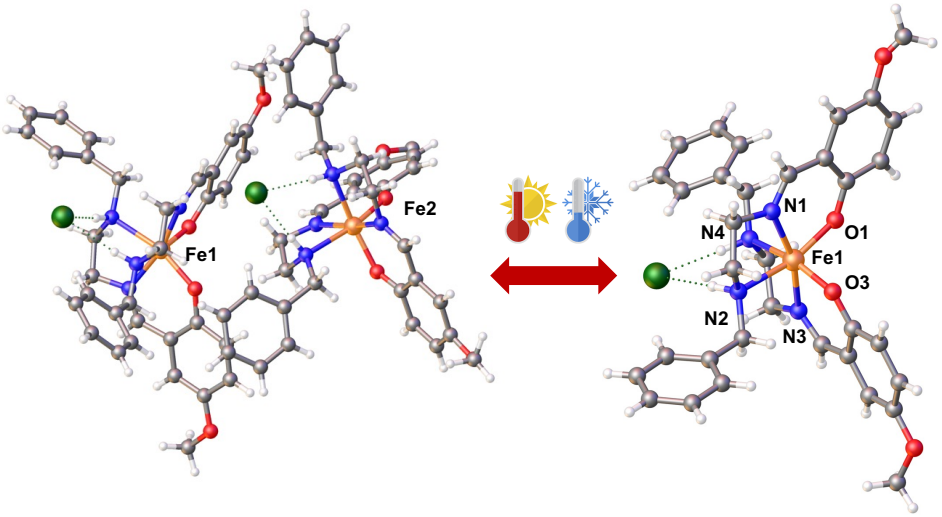

Figure 4.6 View of the asymmetric unit of [Fe(salBzen-5-OMe)$_2$]Cl (**1**) at 150 K (left) and 295 K (right).

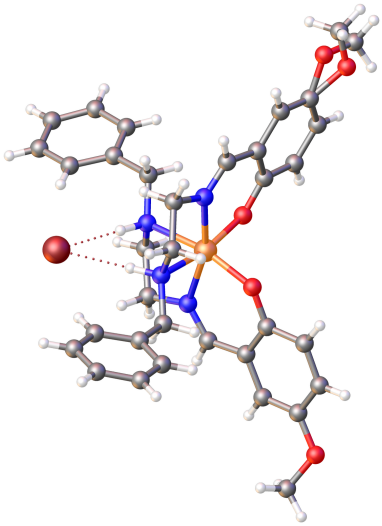

Figure 4.7 View of the asymmetric unit of [Fe(salBzen-5-OMe)$_2$]Br (**2**) at 295 K.

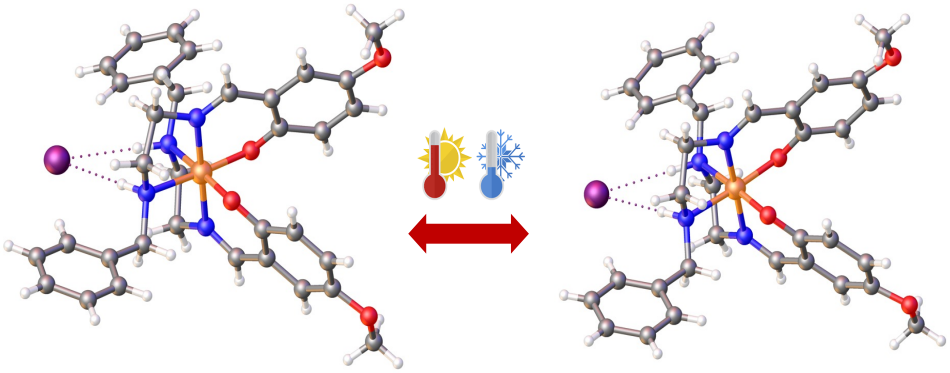

Figure 4.8 View of the asymmetric unit of [Fe(salBzen-5-OMe)$_2$]I (**3**) at 150 K (left) and 295 K (right).

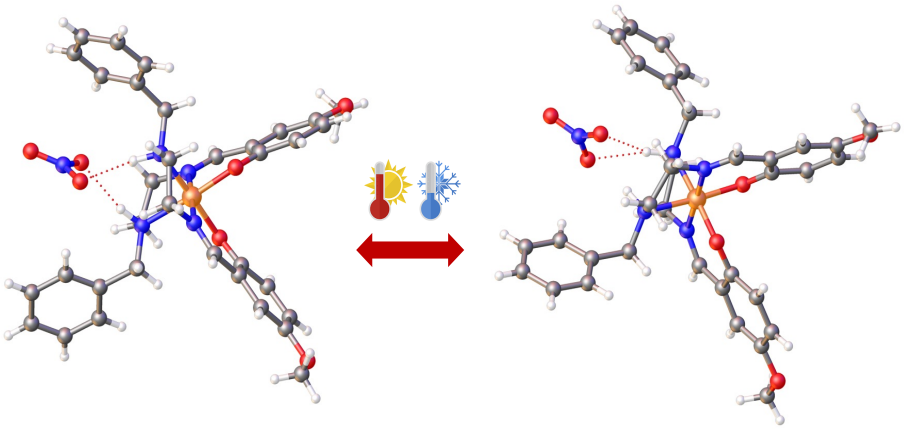

Figure 4.9 View of the asymmetric unit of [Fe(salBzen-5-OMe)$_2$]NO_3 (**4**) at 150 K (left) and 295 K (right).

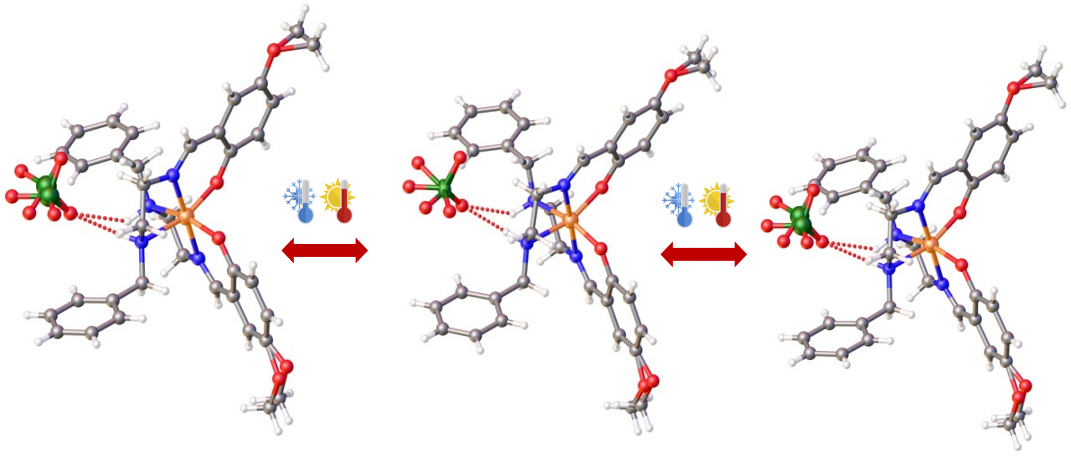

Figure 4.10 View of the asymmetric unit of $[Fe(salBzen\text{-}5\text{-}OMe)_2]ClO_4$ (**5**) at 30 K (left), 100 K (middle) and 290 K (right).

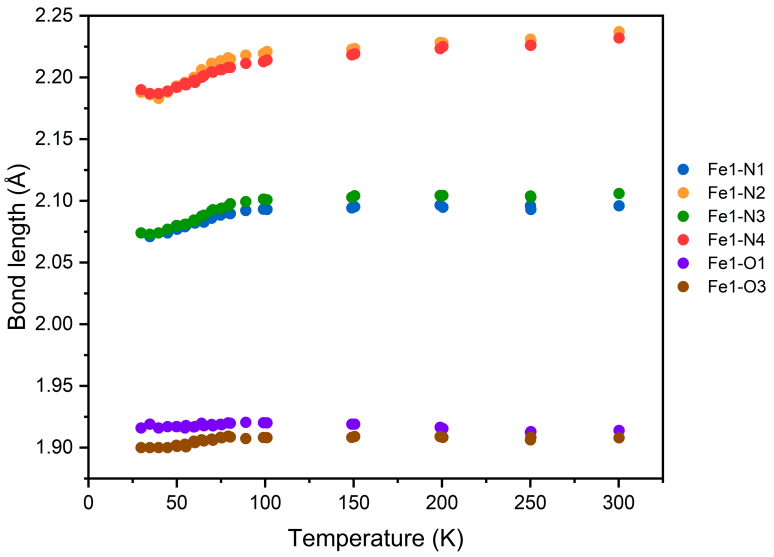

Figure 4.11 Fe-N/O bond lengths (Å) of $[Fe(salBzen\text{-}5\text{-}OMe)_2]ClO_4$ (**5**) at 30-300 K.

Table 4.3 Selected Fe-N/O bond lengths (Å) and octahedral distortion parameters (°) of **1**–**3** complexes.

Fe–N/O bond distance/Å	**1**		**2**	**3**	
T/K	**150**	**295**	**295**	**150**	**295**
Fe1-O1	1.914(18)	1.914(2)	1.904(3)	1.864(6)	1.858(6)
Fe1-O3	1.930(18)	1.915(2)	1.899(3)	1.864(6)	1.858(6)
Fe1-O_{ave}	1.920(18)	1.914(2)	1.902(3)	1.864(6)	1.858(6)
Fe1-N1	2.125(2)	2.108(2)	2.087(3)	1.914(7)	1.925(7)
Fe1-N2	2.217(2)	2.243(2)	2.230(3)	2.065(6)	2.082(7)
Fe1-N3	2.121(2)	2.109(2)	2.085(3)	1.914(7)	1.925(7)
Fe1-N4	2.258(2)	2.237(2)	2.240(3)	2.065(6)	2.082(7)
Fe1-N_{ave}	2.180(2)	2.174(2)	2.161(3)	1.990(7)	2.003(7)
Fe2-O5	1.918(18)				
Fe2-O7	1.923(18)				
Fe2-O_{ave}	1.921(18)				
Fe2-N5	2.107(2)				
Fe2-N6	2.235(2)				
Fe2-N7	2.108(2)				
Fe2-N8	2.232(2)				
Fe2-N_{ave}	2.171(2)				

Table 4.3 Selected Fe-N/O bond lengths (Å) and octahedral distortion parameters (°) of **1**–**3** complexes (Continued).

Σ^{a}Fe1, Fe2	75, 67	68	67	42	41
Θ^{b}Fe1, Fe2	294, 245	270	272	125	129

Table 4.4 Selected Fe-N/O bond lengths (Å) and octahedral distortion parameters (°) of **4** and **5** complexes.

Fe–N/O bond distance/Å	**4**		**5**		
T/K	**150**	**295**	**30**	**100**	**295**
Fe1-O1	1.873(2)	1.864(2)	1.916(3)	1.913(3)	1.908(2)
Fe1-O3	1.867(2)	1.870(2)	1.900(3)	1.920(3)	1.910(2)
Fe1-O_{ave}	1.87(2)	1.86(2)	1.908(3)	1.91(3)	1.90(2)
Fe1-N1	1.931(3)	1.931(2)	2.074(3)	2.097(3)	2.098(2)
Fe1-N2	2.053(3)	2.070(2)	2.188(3)	2.218(3)	2.232(3)
Fe1-N3	1.933(3)	1.932(2)	2.074(3)	2.093(3)	2.101(2)
Fe1-N4	2.060(3)	2.056(2)	2.190(3)	2.217(3)	2.230(3)
Fe1-N_{ave}	1.99(3)	1.99(2)	2.131(3)	2.15(3)	2.16(3)
Σ^{a}Fe1	44	44	68	75	76
Θ^{b}Fe1	128	122	252	268	270

[a] See ref. (Hayami et al., 2000) for a definition. [b] See ref. (McCusker et al., 1996) for a definition

Table 4.5 Crystallographic data and refinement parameters for **1**–**3** complexes.

	1		2	3	
Formula	$C_{34}H_{38}FeClN_4O_4$		$C_{34}H_{38}FeBrN_4O_4$	$C_{34}H_{38}FeIN_4O_4$	
T (K)	150	295	295	150	295
MW	657.99		702.44	749.44	
Radiation	CuKα		MoKα	MoKα	
λ (Å)	1.54184		1.54184	1.54184	
Crystal system	Monoclinic		Monoclinic	Tetragonal	
Space group	$P2_1/c$	$P2_1/n$	$P2_1/n$	$P4_32_12$	
a (Å)	15.2305(1)	10.8769(2)	10.8893(4)	14.4120(3)	14.4413(5)
b (Å)	26.9521(2)	27.1935(4)	26.6396(9)	14.4120(3)	14.4413(5)
c (Å)	15.5275(1)	11.0607(2)	11.2389(4)	15.9501(5)	16.1930(8)
α (°)	90	90	90	90	90
β (°)	91.909(10)	91.7580(10)	91.901(3)	90	90
γ (°)	90	90	90	90	90
Cell volume ($Å^3$)	6370.41(8)	3270.00(10)	3258.5(2)	3312.93(17)	3377.1(3)
Z	8	4	4	4	4
μ (mm^{-1})	4.926	4.796	1.732	1.430	1.403

Table 4.5 Crystallographic data and refinement parameters for **1**–**3** complexes (Continued).

Reflections collected	**36337**	**18478**	**76698**	**30245**	**26876**
Independent reflections, R_{int}	11650, 0.0646	5975, 0.0415	7549, 0.0431	3369, 0.0471	2966, 0.0451
***R*-Factor (%), wR_2 (%)**	5.08, 14.46	4.86, 14.68	5.60, 13.94	5.49, 17.25	5.39, 17.00

Table 4.6 Crystallographic data and refinement parameters for **4** and **5** complexes.

	4		**5**		
Formula	$C_{34}H_{38}FeN_5O_7$		$C_{34}H_{38}FeClN_4O_8$		
T (K)	150	295	30	100	295
MW	684.54		721.98		
Radiation	CuKα		MoKα		
λ (Å)	1.54184		1.54184		
Crystal system	Monoclinic		Monoclinic		
Space group	$P2_1/c$	$P2_1/c$	$P2_1/c$		
a (Å)	12.0908(4)	12.2018(2)	24.1980(9)	24.3441(6)	24.5743(4)
b (Å)	14.2947(4)	24.2085(2)	13.2518(6)	13.3372(2)	13.4596(2)
c (Å)	18.9379(6)	19.4811(3)	10.5331(5)	10.5371(3)	10.6821(2)

Table 4.6 Crystallographic data and refinement parameters for **4** and **5** complexes (Continued).

α (°)	**90**	**90**	**90**	**90**	**90**
β (°)	99.609(3)	99.366(2)	98.553(4)	98.702(2)	98.479(10)
γ (°)	90	90	90	90	90
Cell volume (Å^3)	3227.20(18)	3332.40(9)	3340.1(3)	3381.82(14)	3494.60(10)
Z	4	4	4	4	4
μ (mm^{-1})	4.223	4.090	0.589	1.418	4.629
Reflections collected	16041	19107	50157	17483	17745
Independent reflections, R_{int}	5860, 0.0484	6101, 0.0471	8265, 0.0749	6178, 0.0578	6381, 0.0447
***R*-Factor (%), wR_2 (%)**	5.81, 16.76	5.09, 14.79	7.38, 16.26	6.48, 18.19	5.15, 16.12

Table 4.7 Key intermolecular interactions for **1**–**3** complexes.

	1		**2**	**3**	
T (K)	150	295	295	150	295
NH···A (Å)	2.330	2.255	2.394	2.590	2.613
Normalized NH···A[1]	0.801	0.775	0.785	0.794	0.802
***2-D* sheets on ab plane**					
CH_{imine}···A (Å)	2.898	2.799	2.895	3.038	3.069
Normalized CH···A[1]	0.996	0.962	0.950	0.932	0.941
$CH_{ethylene}$···A (Å)	2.742	2.741	2.818	3.059	3.072
Normalized CH···A[1]	0.942	0.942	0.924	0.938	0.942
$CH_{ethylene}$···**π** (Å)	2.868	2.850	2.862	-	-
Between *2-D* sheets along c-axis					
CH_{ethyl}···**π** (Å)	2.887	2.868	2.887	-	-
CH_{ethyl}···O (Å)	2.907	3.090	3.042	2.569	2.658

[1] Normalized contacts (Hariharan, 2022) were calculated from the ratio of the experimental distances and sum of corresponding van der Waals atomic radii (Mantina et al., 2009) and Pauling ionic radii (Pauling, 1927).

Table 4.8 Key intermolecular interactions for **4** and **5** complexes.

	4		**5**		
T (K)	150	295	30	100	295
NH···A (Å)	2.145	2.167	2.601	2.603	2.646
***2-D* sheets on ab plane**					
CH_{imine}···A (Å)	2.621	2.657	2.583	2.631	2.643
$CH_{ethylene}$···A (Å)	2.670	2.669	2.495	2.694	2.645
$CH_{ethylene}$···**π** (Å)	2.855	2.714	2.574	2.694	2.756
Between *2-D* sheets along c-axis					
CH_{ethyl}···**π** (Å)	-	-	-	-	-
CH_{ethyl}···O (Å)	2.698	-	2.556	2.718	2.707

A feature that all the structures share is that a combination of N–H···anion and C–H···anion interactions link the cations. Notably, in **1** the N–H···Cl contacts at Fe1 and Fe2 differ by only 0.001 Å at 150 K, indicating minimal change. Even at 295 K, where symmetry breaking reduces the structure to a single Fe center, the N–H···Cl distance changes by just 0.07 Å. This stability suggests that the ligand field remains weak and does not strengthen enough to favor the LS state, even when the symmetry is lowered. Additionally, packing in **1** shows the formation of 1D chains of both Fe1 and Fe2 centers at 150 K, with neighboring chains linked through N–H···Cl and C–H···Cl interactions to form 2D sheets in the *ac* plane (Figure 4.12). This dense network appears to resist the contraction typically associated with the LS state, further stabilizing the HS configuration at LT. The electronic environment surrounding the Fe centers, influenced by hydrogen-bonding interactions with the Cl anions, may further contribute to the HS state stability by maintaining a relatively weak ligand field. Thus, despite symmetry breaking, the compound's rigid framework, stable ligand field, and network of intermolecular interactions effectively inhibit SCO, leading to the unusual retention of the HS state at both low and high temperatures. It is noteworthy that the packing closely resembles that of the related compound $[Fe(naphBzen)_2]I$ which exhibits strongly hysteretic SCO and hidden hysteresis as a result of an extremely rare *reverse*-LIESST process (Boonprab et al., 2019). In comparison to the packing in the structure of complex **2**, we observe a distinct square motif (Figure 4.13) that resembles structural features seen in $[Fe(salEen\text{-}5\text{-}I)_2]$halide, particularly $[Fe(salEen\text{-}5\text{-}I)_2]Br$ (Boonprab et al., 2024), which exhibits stepped SCO transition close to room temperature. However, unlike $[Fe(salEen\text{-}5\text{-}I)_2]Br$, complex **2** remains in the HS state even at LT, as evidenced by its magnetic profile (*vide infra*). This persistence of the HS state in **2**, despite structural similarities to SCO-active $[Fe(salEen\text{-}5\text{-}I)_2]Br$, suggests a potentially significant influence of the square arrangement within the lattice. Although the square motif is retained, its specific packing and intermolecular interactions appear to prevent SCO, maintaining the HS state at all observed temperatures. In complex **3**, the crystal lattice at both 295 K and 150 K consistently features a square motif, similar to that in $[Fe(naphBzen)_2]Cl$ and $[Fe(naphBzen)_2]Br$ (Habarakada et al., 2022), but uniquely exhibits a helical arrangement where the square motif spirals out of the 2D plane,

forming a three-dimensional structure (Figure 4.14). This distinctive helical configuration, stabilized by specific anion interactions, sets it apart from the diverse but planar packing patterns observed in the [Fe(naphBzen)$_2$]halide family in different solvates. We observe that the benzyl group of the salBzen ligand has a strong tendency to form a square arrangement with halide anions—a structural characteristic that appears to have been previously unrecognized. In our system, the anion plays a dominant role in stabilizing this arrangement. Both compounds **1** and **2** exhibit a clear square motif, while compound **3** also forms a square arrangement, though it differs in its spiral configuration that extends out of the 2D plane. This distinctive, non-planar arrangement in compound **3** underscores the versatility of the salBzen ligand and highlights the influence of specific anion interactions in directing the formation of unique packing motifs.

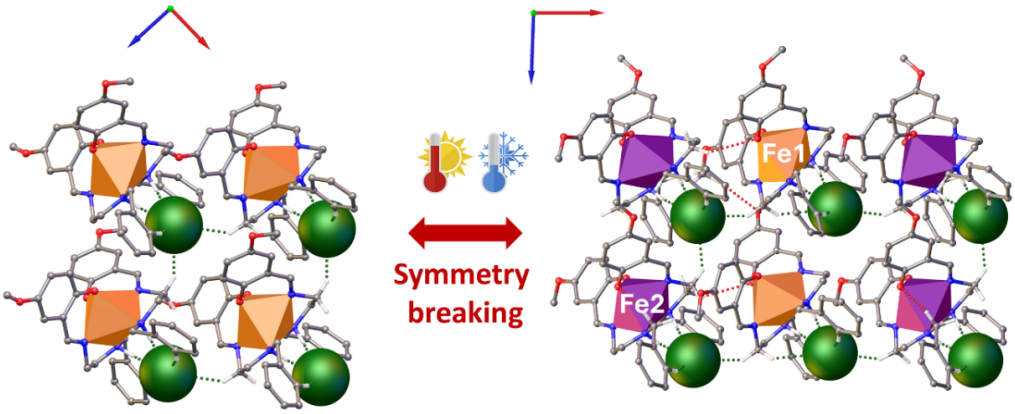

Figure 4.12 Spacefill packing [Fe(salBzen-5-OMe)$_2$]Cl (**1**) at 295 K (left) and 150 K (right) viewed along the *b* axis in HS state.

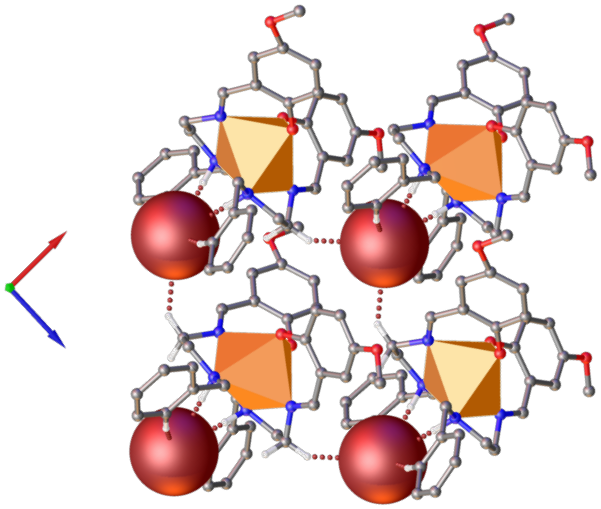

Figure 4.13 Spacefill packing [Fe(salBzen-5-OMe)$_2$]Br (**2**) at 295 K viewed along the *b* axis in HS state.

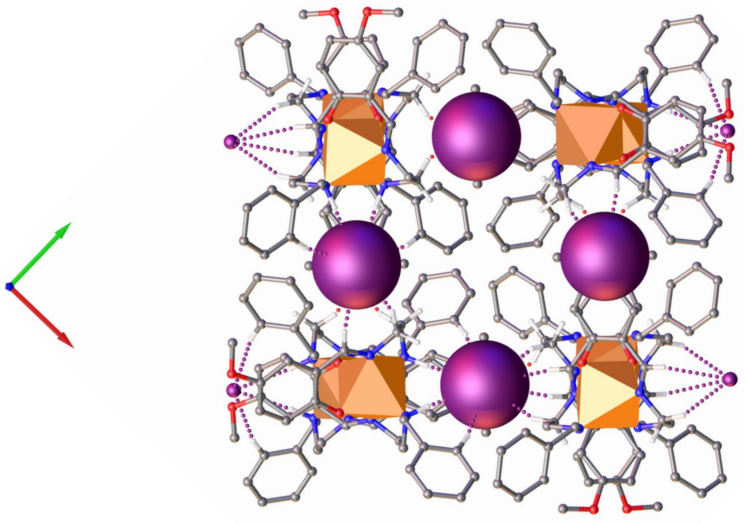

Figure 4.14 Spacefill packing of [Fe(salBzen-5-OMe)$_2$]I (**3**) at 295 K viewed along the *c* axis with LS state.

In complexes **4** and **5**, at 290 K and 30 K respectively, distinct packing patterns emerge compared to the other halide structures. A key feature of these two complexes is the formation of a 3D supramolecular network driven by a combination of C-H···**π**, C-H···O, N-H···O, C-H···anion, and N-H···anion interactions, all involving the anion. In **4**, the Fe centers exhibit a dimer-like arrangement, forming pairs or clusters of complexes

that stack into a brick-like pattern of parallelograms (Figure 4.15). The NO_3 anions act as bridges or spacers, facilitating the dimerization and shaping the parallelogram-based packing motif. These dimeric interactions, likely stabilized by hydrogen bonding and coordination with NO_3 ions, result in an asymmetric yet efficient packing arrangement. Compared to the square motif observed in compound **3**, the structure of complex **4** is less symmetric, with a more layered and staggered arrangement of complexes. For complex **5**, the Fe centers are organized into layers, forming a repeating pattern where the units shift slightly between layers. The ClO_4 ions function as spacers, stabilizing the structure through weak interactions and ionic forces. The packing pattern is defined by a trapezoidal tessellation (Figure 4.16), representing a slight distortion from a perfect square grid. This distortion introduces a layered and slightly offset arrangement, likely influenced by the size and interaction dynamics of the ClO_4 ions.

The comparison of complexes **4** and **5** highlights the significant role of different anions (ClO_4^- and NO_3^-) in influencing packing and symmetry. These observations underscore how subtle variations in the molecular environment can result in diverse and unique packing motifs.

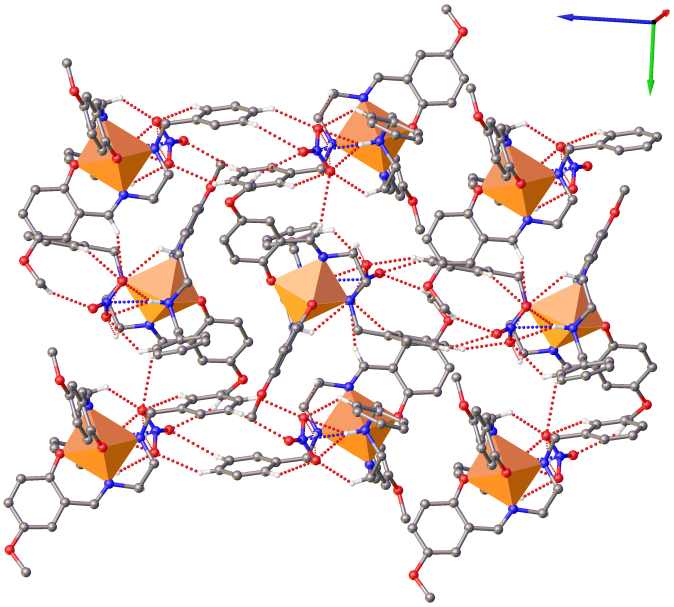

Figure 4.15 Packing of $[Fe(salBzen\text{-}5\text{-}OMe)_2]NO_3$ (**4**) at 295 K viewed along the *c* axis in LS state.

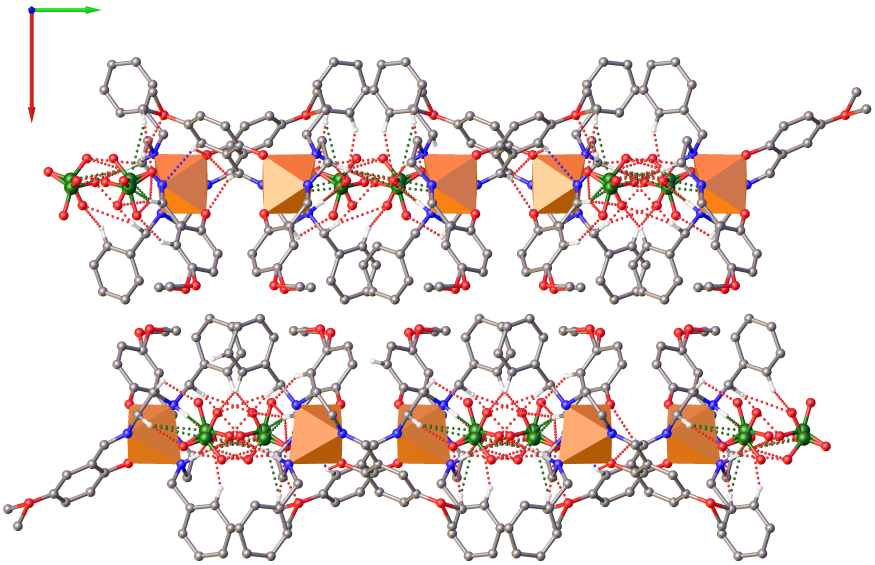

Figure 4.16 Packing of [Fe(salBzen-5-OMe)$_2$]ClO$_4$ (**5**) at 100 K viewed along the *c* axis in HS state.

4.3 Hirshfeld surface data analysis of Fe(III) Schiff base complexes

Hirshfeld surfaces highlight the role of intermolecular interactions in creating a network of contacts between cations and anions, as well as neighboring cations within the crystal lattice. These interactions arise from functional groups associated with the counterions or cations, including N–H, C–H, aromatic rings, and halides. The red regions on the isosurface indicate significant hydrogen bonding at the H···O, H···**π**, and H···H sites. The positioning of counteranions within the lattice promotes C–H···A and N–H···A interactions, with darker red spots reflecting stronger interactions, particularly between C–H and N–H groups and counteranions, as shown in Figure 4.17. In contrast, weaker H···H interactions within the lattice correspond to lighter red regions, while the strength of H···A interactions varies with the electronegativity of the halide.

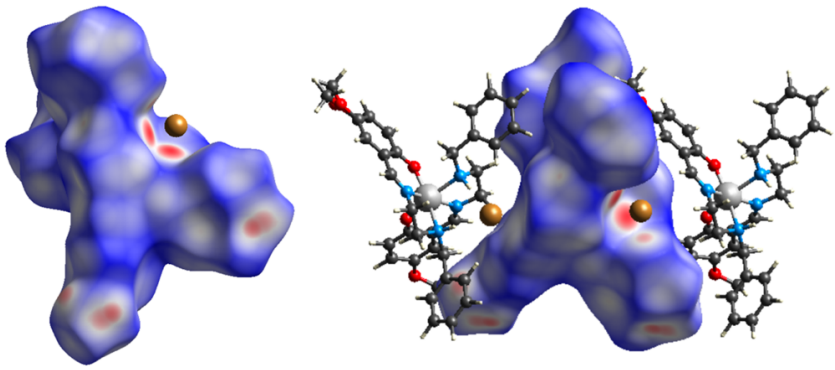

Figure 4.17 Intramolecular interactions (covalent bond) (left) and C–H···**π** interactions (right) through Hirsfeld surface mapping by d_{norm} function.

The Hirshfeld surfaces of compounds **1**-**5** clearly show that C–H···**π** and H···O interactions significantly contribute to the total interactions, accounting for 19.6–27.6% and 7.1–21.6%, respectively. The H···A interactions, influenced by the halides, contribute 5.2–7.4%. The 2D fingerprint plots in Figures 4.18 and 4.19 further illustrate these contributions. Substituents influence spin crossover behavior by altering these interactions. Complexes with Cl^- and Br^- anions show stronger N–H···halide interactions, stabilizing the HS state and preventing SCO. In contrast, the weaker N–H···halide interactions with the larger, more polarizable I^- anion, stabilizing the LS state and leading to a gradual SCO above 350 K. This trend is consistent with the [Fe(salEen-I)$_2$]halide series (Boonprab et al., 2024), where weaker interactions promote the LS state. However, in the [Fe(salEen-I)$_2$]halide series, the SCO occurs with the Br^- anion, whereas in the [Fe(salBzen-5-OMe)$_2$]halide series, it occurs between Br^- and I^-.

Hirshfeld analysis indicates that varying substituents impact the characteristics of the spin crossover. The nature of the counteranion significantly affects the contributions of H···C and H···O interactions. Halide complexes **1**–**3** exhibited comparable H···C and H···O interactions, reflecting the similar sizes and polarizabilities of the halide ligands. However, complexes containing NO_3 **4** and ClO_4 **5** demonstrated significantly enhanced H···O interactions due to the presence of oxygen atoms in the anions capable of forming weak hydrogen bonds. The thermal dependence of these interactions also revealed that the H···O contributions increased with temperature in

these complexes, highlighting the interplay between thermal motion and intermolecular forces.

Hirshfeld analysis confirms that substituents significantly influence SCO behavior by modifying intermolecular interactions and lattice packing. Strongly coordinating anions, such as such as Cl **1** and Br **2**, create a more rigid lattice, leading to a narrower SCO transition range. In contrast, ClO_4 **5**, exhibits only a weak SCO, likely due to disorder in the ClO_4 anion between 80 K and 90 K, which appears to drive the observed transition. Meanwhile, NO_3 **4** behaves more similarly to I **3** than to ClO_4 **5**, suggesting intermediate effects on the SCO process.

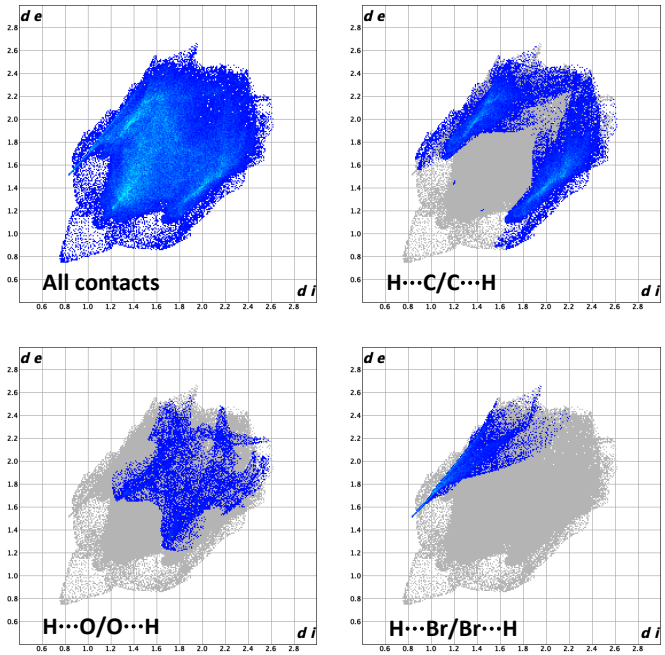

Figure 4.18 2D fingerprint plots of all contacts: H···C, H···H and H···O for **2** at 295 K.

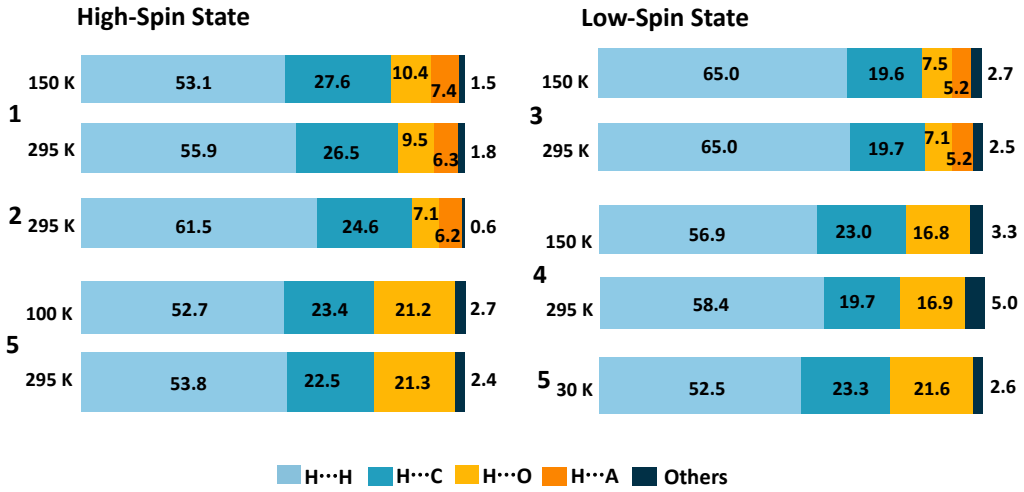

Figure 4.19 Percentage contributions of interactions for complexes **1**-**5**.

4.4 Magnetic studies of Fe(III) Schiff base complexes

The magnetic properties of **1**-**5** were undertaken using SQUID magnetometry over the 10–380 K range and are presented as $\chi_M T$ vs. T plots in Figure 4.20 (χ_M is defined as the magnetic susceptibility, expressed as M/H per mole of the complex). The $\chi_M T$ values for complexes **1** and **2**, which remain in the range of 4.00–4.50 cm^3 K mol^{-1} between 10 and 300 K, and are indicative of HS Fe(III) centers across the entire temperature range, with complex **1** maintaining a $\chi_M T$ value around 4.50 cm^3 K mol^{-1} at all temperatures, in agreement with X-ray crystallographic analysis, and complex **2** exhibits a similar magnetic profile, with a $\chi_M T$ value of 4.40 cm^3 K mol^{-1} at 150 K and remaining HS down to 10 K. These values agree well with Fe(III) complexes within the same ligand family (Al-Azzani et al., 2020; Boonprab et al., 2024; Dey et al., 2020; Marques et al., 2023; Shongwe et al., 2012). In contrast, in the $[Fe(naphBzen)_2]Cl$ and $[Fe(naphBzen)_2]Br$ complexes (Habarakada et al., 2022), different solvates can be obtained through recrystallization from various solvents. Notably, in the $CHCl_3$ solvates, both complexes remain trapped in the LS state. Magnetic data indicate that SCO occurs only in the hexane solvates, highlighting that even very weak interactions can play a critical role in facilitating SCO behavior. It is evident that the naphBzen complexes tend to exhibit very gradual and minimal transitions, resulting in predominantly mixed HS

and LS states. This telling us the salBzen ligand is substantially more HS than the naphBzen and naphEen ligands.

In contrast, the χ_MT value of **3** is around 0.52 cm^3 K mol^{-1} at 100 K and aligns with an LS Fe(III) center, supporting agreement with X-ray crystallograhic analysis. Upon heating of **3** undergoes a gradual and smooth spin crossover, reaching χ_MT of 2.09 cm^3 K mol^{-1} at 380 K, this suggests that the spin crossover remains incomplete at this temperature (Boonprab et al., 2018; Marques et al., 2023; Martinho et al., 2014; Vicente et al., 2016). Similarly, complex **4** displays a χ_MT value of 0.46 cm^3 K mol^{-1} at 100 K, also consistent with a LS Fe(III) centre and agrees well with SCXRD. Upon heating, the χ_MT value begins to slightly increase, reaching 1.38 cm^3 K mol^{-1} at 380 K, which is slightly lower than that of complex **3**. These profiles suggest that both compounds **3** and **4** exhibit predominantly gradual spin crossover above 350 K. Similar behavior has been reported in in $[Fe(salEen\text{-}5\text{-}I)_2]I$ (Boonprab et al., 2024), which shows a gradual and incomplete SCO from LS to mHS over the examined temperature range. Notably, the $T_{1/2}$ values recorded for $[Fe(salEen\text{-}5\text{-}I)_2]$halide (Boonprab et al., 2024) increase as the anionic radii increases, suggesting that bigger anions stabilize the LS state — a trend consistent with our system, $[Fe(salBzen\text{-}5\text{-}OMe)_2]A$, as it moves from chloride to iodide. For complex **5**, the χ_MT value is around 4.42 cm^3 K mol^{-1} at 300 K indicating that the complex is almost fully HS. Upon cooling down to 100 K, the χ_MT value remains around 4.35 cm^3 K mol^{-1}, confirming that the complex stays in the HS Fe(III) state, consistent with SCXRD results. However, the χ_MT value drops abruptly below 70 K, reaching about 3.50 cm^3 K mol^{-1}, indicating a partial SCO, which aligns with the structural data. Continued cooling causes no significant variation in the χ_MT value, and upon reheating, the spin crossover resumes abruptly, beginning at 60 K. Consequently, the spin transition occurs with a slight hysteresis of 6 K., corresponding to 20% switching of the Fe(III) centres. Notably, such a spin transition with hysteresis at very low temperatures is highly unusual in spin crossover chemistry, especially for Fe(III). This behavior suggests that the salBzen ligand system, combined with appropriate anions, offer a valuable tool for tuning the temperature at which spin crossover occurs.

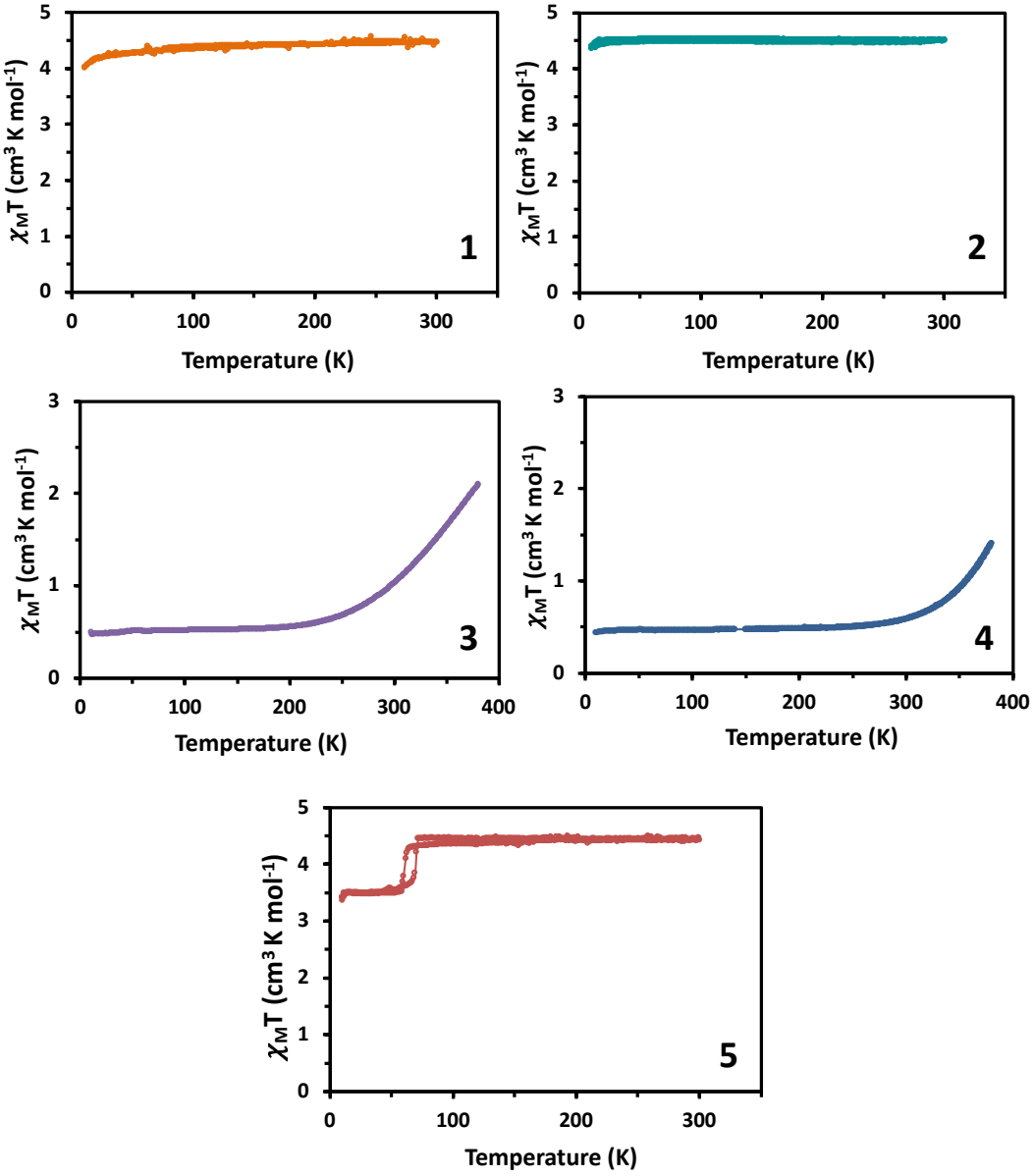

Figure 4.20 $\chi_M T$ versus T plots for 1–5 complexes.

The magnetic properties of complexes **6**-**10** were investigated using direct current (dc) susceptibility and magnetization measurements. These measurements were conducted on a Quantum Design MPMS 3 SQUID magnetometer over the temperature range of 1.8–300 K or 1.8–400 K. The measurement protocol involved four sequential steps: cooling from 300 to 1.8 K (cooling 1), before measuring to 400 K (heating 1), followed by measurement to 1.8 K (Cooling 2), followed by measurement to 400 K (heating 2). Magnetisation (M) vs field (H) measurements were conducted between 0 and 7 T at 1.8, 4 and 7 K, as shown in Figure 4.21.

The variation of magnetic susceptibility with temperature, $\chi_M T$, was measured during both cooling and heating cycles across the 2–400 K range. The data reveal a gradual increase in $\chi_M T$ with increasing temperature for all complexes, indicating temperature-driven spin-state transitions on the Fe(III) centers. The first magnetic profile is different to the next one suggesting an irreversible change (probably solvent water loss). At high temperatures (above ~300 K), all complexes display $\chi_M T$ values converging toward 3.5–4.0 cm^3 K mol^{-1}, consistent with a high-spin state of Fe(III) in a weak-field environment. However, significant differences emerge in the low-temperature region. Complexes **6** and **7** exhibit nearly identical magnetic behavior across the entire temperature range, reflecting the similar crystal field strengths and electronic environments provided by these halide anions. In contrast, complex **8** shows a slightly lower $\chi_M T$ values at low temperatures, potentially due to the larger size of the iodide, which may stabilize a partial low-spin state or promote antiferromagnetic interactions. Complexes **9** and **10** exhibit higher $\chi_M T$ values in the low-temperature region compared to the halide-containing complexes. This behavior is likely due to the weaker intermolecular interactions of NO_3 and ClO_4 anions, which lead to reduced stabilization of the low-spin state. These findings highlight the role of counteranion size and interaction strength in governing the SCO behavior of Fe(III) Schiff base complexes.

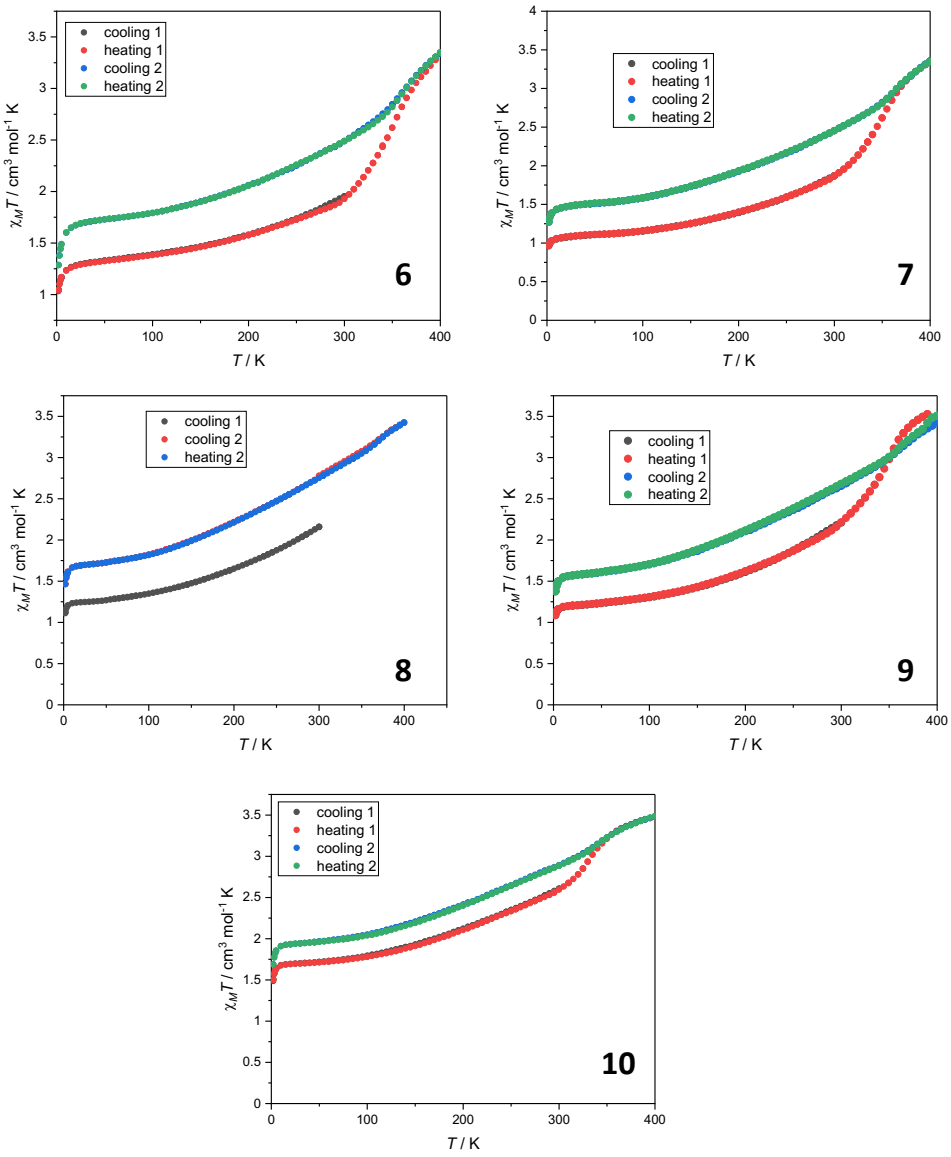

Figure 4.21 χ_MT versus T plots for **6**–**10** complexes.

4.5 Magnetostructural Relationship of Fe(III) complexes

To gain deeper insight into the varying SCO profiles of the complexes, the packing arrangements within their structures were analyzed. In complexes **1**-**3**, the molecular packing is primarily governed by strong N–H···anion and C–H···anion interactions, resulting in the formation of two-dimensional (2D) sheets. The normalized N–H···anion contacts range from 0.77 to 0.80 (Table 4.7), whereas the C–H···anion interactions are comparatively weaker, with normalized contact values close to 1.0. However, these interactions slightly strengthen during the gradual SCO in complex **3**. The helical chain formed by these interactions stack along the c-axis through weak C–H···**π** and C–H···O interactions, suggesting that the most significant contacts occur within the helical chain themselves.

To analyze structural changes related to magnetic profiles, three characteristics (**A**–**C**) similar to those we previously defined for [Fe(salEen-I)$_2$]halide (Boonprab et al., 2024), were created to describe the square configuration of the cationic complexes surrounding the anion within the sheets, as shown in Figure 4.22. These parameters show an increase with the size of the anion, regardless of the spin state, highlighting the lattice space occupied by each anion (Table 4.9). For complexes **1** and **2**, the smaller values of **A**–**C** suggest a threshold below which SCO cannot occur. In contrast, complex **3** shows an increase in these parameters with temperature, indicating tighter trapping of the anion during SCO. This behavior aligns with the more gradual SCO observed in complex **3**.

In comparison, the previously studied [Fe(salEen-I)$_2$]halides exhibited a different trend. For these complexes, **A**–**C** parameters decreased with increasing temperature during SCO, reflecting lattice contraction as the anion became more tightly confined. This trend was particularly pronounced in [Fe(salEen-I)$_2$]Br, where sharp decreases in parameters **B** and **C** (by 0.31 and 0.15 Å, respectively) between 275 and 280 K corresponded to the initial step in the SCO profile, while a subsequent reduction in **A** (~0.2 Å) correlated with the more abrupt SCO transition. In contrast, [Fe(salEen-I)$_2$]I displayed only subtle changes in **A**–**C** (less than 0.1 Å), consistent with its compact packing and gradual SCO (Boonprab et al., 2024). These comparisons highlight that the gradual SCO behavior observed in complex **3** arises from greater lattice flexibility and

enhanced anion-cation interactions. This contrasts with the rigid structural response of [Fe(salEen-I)$_2$]halides, where abrupt SCO transitions dominate due to tighter lattice confinement and reduced flexibility.

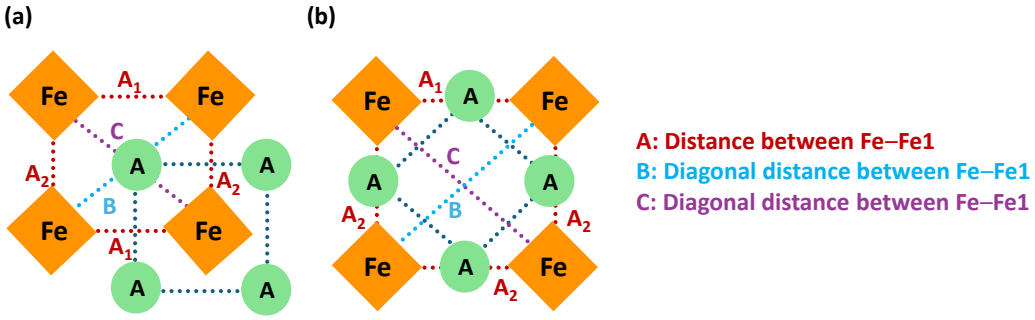

Figure 4.22. (a) Simplified illustration of **1**–**2** and (b) **3** viewed showing the three structural parameters, A_1, A_2, B and C.

Table 4.9 Structural characteristics of complexes **1**–**3**.

Complexes	Structural characteristic (Å)			
	A_1	A_2	B	C
[Fe(salBzen-5-OMe)$_2$]Cl **1**				
150 K	7.329	7.773	10.293	11.061
295 K	7.875	7.637	10.887	11.061
[Fe(salBzen-5-OMe)$_2$]Br **2**				
295 K	7.954	7.694	10.889	11.239
[Fe(salBzen-5-OMe)$_2$]I **3**				
150 K	11.378	10.530	15.923	14.412
295 K	11.426	10.565	16.001	14.441
	A		B	C
[Fe(salEen-5-I)$_2$]Cl				
150 K	7.481		9.85	11.26

Table 4.9 Structural characteristics of complexes **1**–**3** (Continued).

[Fe(salEen-5-I)$_2$]Br			
123 K	7.970	10.75	11.77
275 K	7.985	10.70	11.75
280 K	7.947	10.39	11.60
293 K	7.773	10.37	11.58
305 K	7.776	10.37	11.58
[Fe(salEen-5-I)$_2$]I			
293 K	8.273	11.33	12.06
400 K	8.239	11.30	11.99
425 K	8.239	11.30	11.99

4.6 Cyclic voltammetric studies of Fe(III) Schiff base complexes

The electrochemistry of [Fe(salBzen-5-OMe)$_2$]A, **1**-**5** in dry CH_2Cl_2 was studied using cyclic voltammetry. The cyclic voltammogram of all the complexes are shown in Figures 4.23 and 4.24. The CV measurements, conducted over the potential range of -1.0 to 1.2 V, exhibit distinct redox features corresponding to both metal-centered and ligand-centered electron transfer processes. All complexes display a quasi-reversible Fe(III)/Fe(II) redox couple, with the reduction of Fe(III) to Fe(II) observed during the cathodic scan between -0.50 to -0.35 V and oxidation during the anodic scan at around 0.9-1.0 V, assigned to the salBzen-5-OMe ligand, specifically oxidation at the oxygen of the phenolate (Harding et al., 2013). The potentials of the Fe(II)/Fe(III) redox couple varies a lot from -0.55 V to -0.39 V with a clear relationship between the strength of the N–H···A interactions and the size of the anion. Moreover, for **3** two extra redox events occur and are attributed to the redox reactions of I^-/I_3^- and I_2/I_3^-, the redox peaks on the left correspond to Eq. (1), while those on the right correspond to Eq. (2) (Ma et al., 2021).

$$I_3^- + 2e^- \rightarrow 3\ I^- \qquad (1)$$

$$3I_2 + 2e^- \rightarrow 2\ I_3^- \qquad (2)$$

The reduction potentials for the Fe(II)/Fe(III) redox couple demonstrate how the hydrogen bonding strength of the counteranion affects the stability of the Fe(III) oxidation state. Complex **1**, exhibits the most negative potential (-0.55 V), reflecting the strong stabilizing effect of Cl^- on Fe(III). In comparison, **2** (-0.47 V) and **3** (-0.39 V) complexes display less negative potentials, consistent with the weaker hydrogen bonding capability of these larger halides of Br^- and I^-, respectively. Additionally, two distinct trends emerge when comparing halide and non-halide counteranions. Complex **4** (-0.52 V) has a reduction potential close to that of complex **1**, suggesting that multiple N–H···O hydrogen bonds significantly contribute to Fe(III) stabilization. In contrast, complex **5** (-0.42 V) has the least negative potential, showing that the larger anion interacts weakly with the complex. These trends highlight how both the size and hydrogen bonding capability influence the redox properties of these Fe(III) complexes.

The ligand oxidation potentials are mostly unchanged across all complexes, showing that counteranions have little effect on the ligand's electronic properties. Complex **3** has the highest oxidation potential (1.00 V), suggesting the weakest electron-withdrawing influence. Complexes **2** (0.96 V) and **1** (0.91 V) show slightly lower values due to stronger electron-withdrawing effects that stabilize the oxidized ligand. Similarly, **4** (0.92 V) and **5** (0.96 V) have moderate oxidation potentials, confirming their minimal impact. This consistency supports the idea that the anions mainly stabilize the metal center rather than significantly altering the ligand's redox properties.

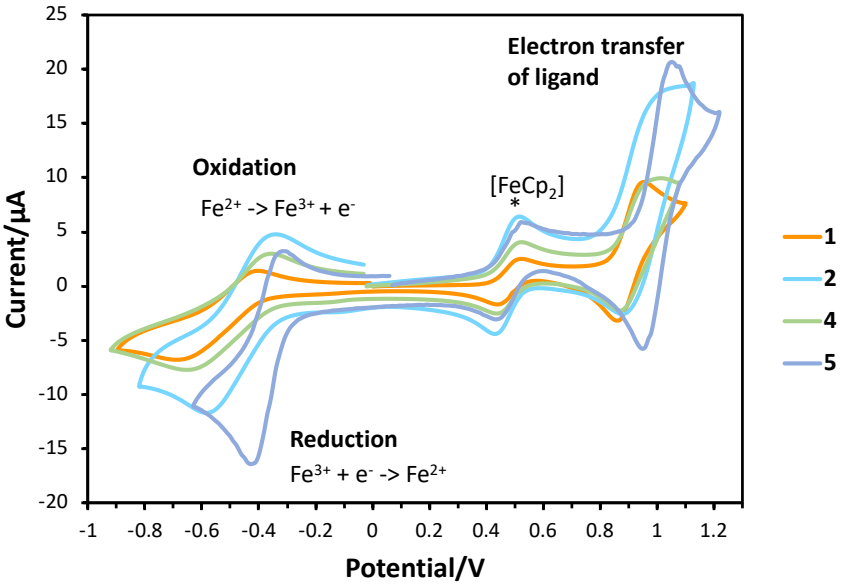

Figure 4.23 Cyclic voltammograms of [Fe(salBzen-5-OMe)$_2$]A in CH_2Cl_2 solution at a scan rate of 100 mVs^{-1}.

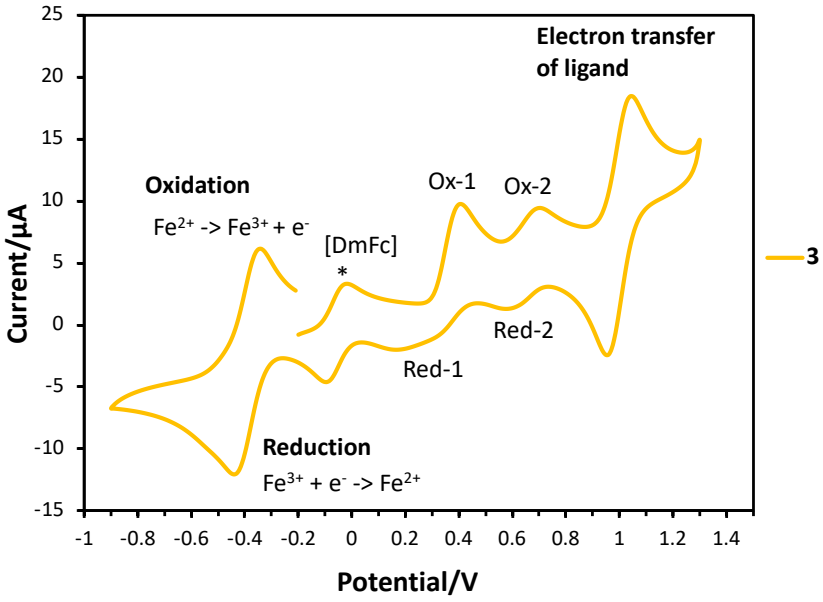

Figure 4.24 Cyclic voltammogram of [Fe(salBzen-5-OMe)$_2$]I in CH_2Cl_2 solution at a scan rate of 100 mVs^{-1}.

Table 4.10 Electrochemical data of [Fe(salBzen-5-OMe)$_2$]A in CH_2Cl_2 solution at 298 K.

Complex[a]	$E^{o'}$ [V] ($Fe^{2+/3+}$)	$E^{o'}$ [V] (ligand)
1	-0.55[b]	0.91[c]
2	-0.47	0.96
3	-0.39	1.00
4	-0.52	0.92
5	-0.42	0.96

[a] All measurements were conducted at 298 K in dried and degassed CH_2Cl_2 0.1 M $[NBu_4][PF_6]$ solution; scan rate 100 mVs^{-1}.

[b] This corresponds to the peak potential.

[c] The first reduction peak potential is used to determine $E^{o'}$.

The electrochemistry of [Fe(salPren-5-OMe)$_2$]A, **6-10** in dry CH_2Cl_2 was studied by using cyclic voltammetry. The cyclic voltammogram of all the complexes is given in Figures 4.25 and 4.26 which also revealed distinct redox behavior influenced by the counteranion. Moreover, for **8** there are exhibit two pairs of oxidation-reduction peaks, which are attributed to the redox reactions of I^-/I_3^- and I_2/I_3^-, the redox peaks on the left correspond to Eq. (1), while those on the right correspond to Eq. (2) (Ma et al., 2021). The reduction potentials for the Fe(II)/Fe(III) redox couple are relatively consistent across the complexes, ranging from -0.49 V to -0.46 V. Complex **6** shows a slightly more negative potential at -0.47 V, indicating a slightly stronger stabilizing effect on Fe(III) compared to Br^- **7**, I^- **8**, and ClO_4^- **10**. The ligand oxidation potentials occur around 0.9 V, corresponding to oxidation within the Schiff base ligand's aromatic system. The second peak, appearing at higher potentials around 1.3 V, likely involves a subsequent ligand oxidation. The first oxidation process occurs in a narrow range between 0.91 V (**10**) and 0.95 V (**6** and **7**). The similarity across this redox process suggests limited influence of the counteranions on the first oxidation state of the ligand. However, in the second oxidation process, variations are more pronounced. The Cl^- complex **6** exhibits the highest potential (1.38 V), followed closely by Br^- **7** (1.37 V),

NO_3^- **9** (1.34 V), ClO_4^- **10** (1.32 V), and I^- **8** (1.30 V). The reasons for this difference are unclear.

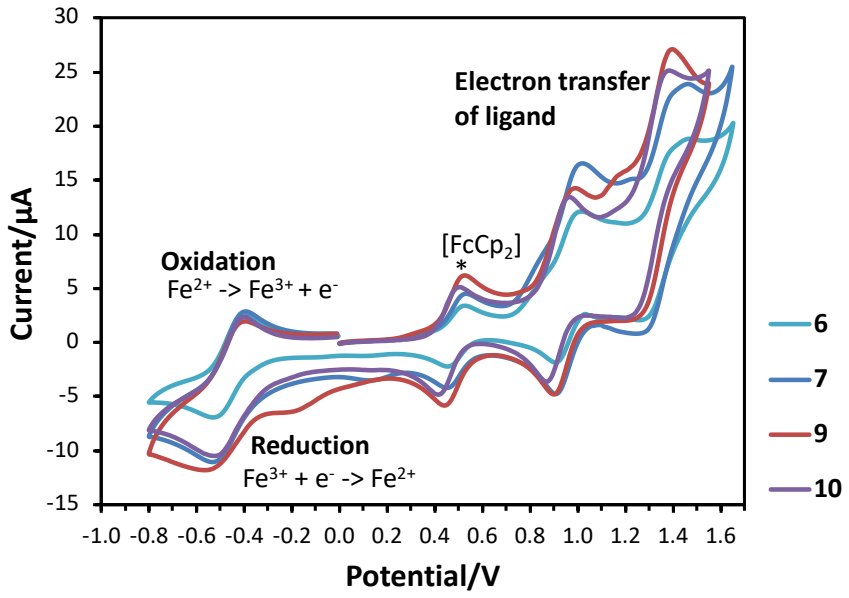

Figure 4.25 Cyclic voltammograms of [Fe(salPren-5-OMe)$_2$]A in CH_2Cl_2 solution at a scan rate of 100 mVs^{-1}.

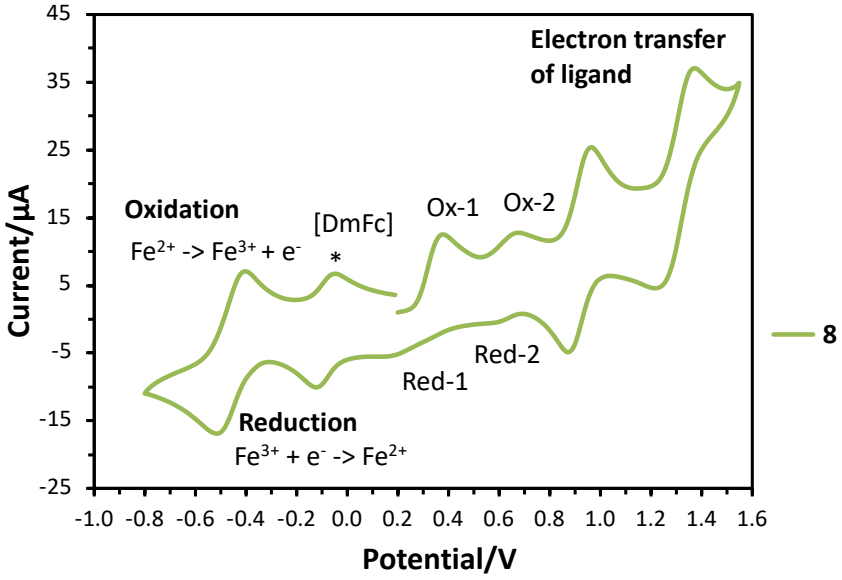

Figure 4.26 Cyclic voltammograms of [Fe(salPren-5-OMe)$_2$]I in CH_2Cl_2 solution at a scan rate of 100 mVs^{-1}.

Table 4.11 Electrochemical data of [Fe(salPren-5-OMe$_2$)$_2$]A in CH_2Cl_2 solution at 298 K.

Complex[a]	$E^{o'}$ [V] ($Fe^{2+/3+}$)	$E^{o'}$ [V] (ligand-p1)	$E^{o'}$ [V] (ligand-p2)
6	-0.47[b]	0.95[c]	1.38[c]
7	-0.46	0.95	1.37
8	-0.46	0.92	1.30
9	-0.49	0.94	1.34
10	-0.46	0.91	1.32

[a] All measurements were conducted at 298 K in dried and degassed CH_2Cl_2 0.1 M [NBu_4][PF_6] solution; scan rate 100 mVs^{-1}.

[b] This corresponds to the peak potential.

[c] The first reduction peak potential is used to determine $E^{o'}$.

The comparison between [Fe(salPren-5-OMe$_2$)$_2$]A, **6**–**10** and [Fe(salBzen-5-OMe$_2$)$_2$]A, **1**–**5** complexes highlights the impact of ligand structure and counteranions on electrochemical behavior. The salBzen series exhibits greater variation in redox potentials depending on the counteranion, likely because the benzyl groups create a more well defined binding pocket that strengthens anion-dependent redox shifts. In contrast, the salPren series shows more consistent redox potentials across different anions, suggesting that its more flexible ligand structure allows greater anion mobility, reducing direct stabilization of the Fe(III) center. These findings emphasize the crucial role of ligand rigidity and counteranion interactions in modulating the redox properties and electron transfer dynamics of Fe(III) Schiff base complexes.

4.7 References

Al-Azzani, M. A., Al-Mjeni, F., Mitsuhashi, R., Mikuriya, M., Al-Omari, I. A., Robertson, C. C., Bill, E., and Shongwe, M. S. (2020). Unusual Magneto-Structural Features of the Halo-Substituted Materials [FeIII(5-X-salMeen)$_2$]Y: a Cooperative [HS-HS]<->[HS-LS] Spin Transition. *Chemistry – A European Journal*, *26*(21), 4766–4779. doi: https://doi.org/10.1002/chem.201904744

Bertrand, J. A., Breece, J. L., and Eller, P. G. (1974). Structure studies of iron(III) salicylaldimine complexes. Five-coordinate monomeric and dimeric complexes. *Inorganic Chemistry*, *13*(1), 125–131. doi: 10.1021/ic50131a024

Boonprab, T., Harding, P., Murray, K. S., Phonsri, W., Telfer, S. G., Alkaş, A., Ketkaew, R., Tantirungrotechai, Y., Jameson, G. N. L., and Harding, D. J. (2018). Solvatomorphism and anion effects in predominantly low spin iron(III) Schiff base complexes. *Dalton Trans.*, *47*(35), 12449–12458. doi: 10.1039/C8DT02016G

Boonprab, T., Lee, S. J., Telfer, S. G., Murray, K. S., Phonsri, W., Chastanet, G., Collet, E., Trzop, E., Jameson, G. N. L., Harding, P., and Harding, D. J. (2019). The First Observation of Hidden Hysteresis in an Iron(III) Spin-Crossover Complex. *Angewandte Chemie International Edition*, *58*(34), 11811–11815. doi: https://doi.org/10.1002/anie.201907619

Boonprab, T., Thammasangwan, W., Chastanet, G., Gonidec, M., Harding, P., and Harding, D. J. (2024). Halide Anion Effects and Magnetostructural Relationships in Iron(III) Spin Crossover Complexes. *Crystal Growth & Design*, *24*, 8145-8152. doi: 10.1021/acs.cgd.4c01068

Cardoso, B. de P., Vicente, A. I., Ward, J. B. J., Sebastião, P. J., Chávez, F. V., Barroso, S., Carvalho, A., Keely, S. J., Martinho, P. N., and Calhorda, M. J. (2015). Fe(III) salEen derived Schiff base complexes as potential contrast agents. *Inorganica Chimica Acta*, *432*, 258–266. doi: https://doi.org/10.1016/j.ica.2015.04.026

Dey, B., Mondal, A., and Konar, S. (2020). Effect of Ligand Field Strength on the Spin Crossover Behaviour in 5-X-SalEen (X=Me, Br and OMe) Based Fe(III) Complexes. *Chemistry – An Asian Journal*, *15*(11), 1709–1721. doi: https://doi.org/10.1002/asia.202000156

Díaz-Torres, R., Phonsri, W., Murray, K. S., Liu, L., Ahmed, M., Neville, S. M., Harding, P., and Harding, D. J. (2020). Spin Crossover in Iron(III) Quinolylsalicylaldiminates: The Curious Case of [Fe(qsal-F)$_2$](Anion). *Inorganic Chemistry*, *59*(18), 13784–13791. doi: 10.1021/acs.inorgchem.0c02201

Habarakada, U., Boonprab, T., Harding, P., S. Murray, K., Phonsri, W., M. Neville, S., Ahmed, M., and J. Harding, D. (2022). Solvent Effects on the Structural and Magnetic Properties of FeIII Spin-Crossover Complexes. *Crystal Growth & Design*, *22*(8), 4895–4905. doi: 10.1021/acs.cgd.2c00390

Harding, D. J., Sertphon, D., Harding, P., Murray, K. S., Moubaraki, B., Cashion, J. D., and Adams, H. (2013). FeIII Quinolylsalicylaldimine Complexes: A Rare Mixed-Spin-State Complex and Abrupt Spin Crossover. *Chemistry – A European Journal*, *19*(3), 1082–1090. doi: https://doi.org/10.1002/chem.201202053

Hariharan, M. (2022). Virtual Issue on Halogen Bonding. *Crystal Growth & Design*, *22*(4), 2046–2049. doi: 10.1021/acs.cgd.2c00157

Hayami, S., Gu, Z., Shiro, M., Einaga, Y., Fujishima, A., and Sato, O. (2000). First Observation of Light-Induced Excited Spin State Trapping for an Iron(III) Complex. *Journal of the American Chemical Society*, *122*(29), 7126–7127. doi: 10.1021/ja001406e

Kang, B., Tang, H., Zhao, Z., and Song, S. (2020). Hofmeister Series: Insights of Ion Specificity from Amphiphilic Assembly and Interface Property. *ACS Omega*, *5*(12), 6229–6239. doi: 10.1021/acsomega.0c00237

Ketkaew, R., Tantirungrotechai, Y., Harding, P., Chastanet, G., Guionneau, P., Marchivie, M., and Harding, D. J. (2021). OctaDist: a tool for calculating distortion parameters in spin crossover and coordination complexes. *Dalton Transactions*, *50*(3), 1086–1096. doi: 10.1039/D0DT03988H

Ma, J., Liu, M., He, Y., and Zhang, J. (2021). Iodine Redox Chemistry in Rechargeable Batteries. *Angewandte Chemie International Edition*, *60*. doi: 10.1002/anie.202009871

Mantina, M., Chamberlin, A. C., Valero, R., Cramer, C. J., and Truhlar, D. G. (2009). Consistent van der Waals Radii for the Whole Main Group. *The Journal of Physical Chemistry A*, *113*(19), 5806–5812. doi: 10.1021/jp8111556

Marques, R. T., Ferreira, L. P., Gomes, C. S. B., Lopes, C. S. D., Bernardes, C. E. S., Sarangi, N. K., Keyes, T. E., and Martinho, P. N. (2023). Reversible Single-Crystal-to-Single-Crystal Transformations in a salEen Fe(III) Spin Crossover Sponge. *Crystal Growth & Design*, *23*(5), 3222–3229. doi: 10.1021/acs.cgd.2c01405

Martinho, P. N., Vicente, A. I., Realista, S., Saraiva, M. S., Melato, A. I., Brandão, P., Ferreira, L. P., and De Deus Carvalho, M. (2014). Solution and solid state properties of Fe(III) complexes bearing N-ethyl-N-(2-aminoethyl)salicylaldiminate ligands. *Journal of Organometallic Chemistry*, *760*, 48–54. doi: https://doi.org/10.1016/j.jorganchem.2013.12.028

McCusker, J. K., Rheingold, A. L., and Hendrickson, D. N. (1996). Variable-Temperature Studies of Laser-Initiated $^5T_2 \longrightarrow {}^1A_1$ Intersystem Crossing in Spin-Crossover Complexes: Empirical Correlations between Activation Parameters and Ligand Structure in a Series of Polypyridyl Ferrous Complexes. *Inorganic Chemistry*, *35*(7), 2100–2112. doi: 10.1021/ic9507880

Pauling, L. (1927). THE SIZES OF IONS AND THE STRUCTURE OF IONIC CRYSTALS. *Journal of the American Chemical Society*, *49*(3), 765–790. doi: 10.1021/ja01402a019

Petty, R. H., Dose, E. V, Tweedle, M. F., and Wilson, L. J. (1978). Bis(N-methylethylene diaminesalicylaldiminato)iron(III) complexes. Magnetic, Moessbauer, and intersystem crossing rate studies in the solid and solution states for a new (S = 1/2) .dblarw. (S = 5/2) spin-equilibrium case. *Inorganic Chemistry*, *17*(4), 1064–1071. doi: 10.1021/ic50182a053

Shongwe, M. S., Al-Zaabi, U. A., Al-Mjeni, F., Eribal, C. S., Sinn, E., Al-Omari, I. A., Hamdeh, H. H., Matoga, D., Adams, H., Morris, M. J., Rheingold, A. L., Bill, E., and Sellmyer, D. J. (2012). Accessibility and Selective Stabilization of the Principal Spin States of Iron by Pyridyl versus Phenolic Ketimines: Modulation of the $^6A_1$ <-> $^2T_2$ Ground-State Transformation of the $[FeN_4O_2]^+$ Chromophore. *Inorganic Chemistry*, *51*(15), 8241–8253. doi: 10.1021/ic300732r

Tweedle, M. F., and Wilson, L. J. (1976). Variable spin iron(III) chelates with hexadentate ligands derived from triethylenetetramine and various salicylaldehydes. Synthesis, characterization, and solution state studies of a new 2T .dblarw. 6A

spin equilibrium system. *Journal of the American Chemical Society*, *98*(16), 4824–4834. doi: 10.1021/ja00432a023

Vicente, A. I., Joseph, A., Ferreira, L. P., de Deus Carvalho, M., Rodrigues, V. H. N., Duttine, M., Diogo, H. P., da Piedade, M. E., Calhorda, M. J., and Martinho, P. N. (2016). Dynamic spin interchange in a tridentate Fe(iii) Schiff-base compound. *Chemical Science*, *7*(7), 4251–4258. doi: 10.1039/C5SC04577K